JOURNAL OF AIRCRAFT
Vol. 36, No. 5, September–October 1999

Experimental Investigation of Simulated Large-Droplet Ice Shapes on Airfoil Aerodynamics

Sam Lee* and Michael B. Bragg†
University of Illinois at Urbana–Champaign, Urbana, Illinois 61801

An experimental investigation was conducted to study the aerodynamic effect of simulated supercooled large-droplet ice accretion on a modified NACA 23012 airfoil. Forward-facing quarter-round simulations with height-to-chord ratios of 0.0083 and 0.0139 were used at a Reynolds number of 1.8×10^6. When the simulated ice was placed at critical chordwise locations, a long separation bubble formed downstream of the simulated ice shape and effectively eliminated the formation of a large leading-edge suction peak that was observed on the clean NACA 23012 airfoil. This resulted in a dramatic reduction in the maximum lift coefficient, as low as 0.27, when the larger simulated ice shape was located at 12% chord. Because the airfoil loading distribution was severely altered, large changes in airfoil pitching moments and flap-hinge moments were also observed.

Nomenclature

C_d = drag coefficient
C_h = flap-hinge-moment coefficient
$C_{h,\alpha}$ = flap-hinge-moment curve slope
C_l = lift coefficient
$C_{l,\max}$ = maximum lift coefficient
$C_{l,\alpha}$ = lift curve slope
C_m = pitching-moment coefficient
$C_{m,\alpha}$ = pitching-moment curve slope
C_p = pressure coefficient
c = model chord
k = protuberance height
Re = Reynolds number based on airfoil chord
x = model coordinate in chordwise direction
y = model coordinate perpendicular to chord
α = angle of attack

Introduction

THE crash of an ATR-72 commuter aircraft near Roselawn, Indiana, on October 31, 1994, has led to much reevaluation of our current understanding of aircraft icing. The accident is thought to have occurred because of the presence of freezing drizzle, which consisted of droplet diameters much larger (50–500 μm) than those in the FAR Part 25, Appendix C icing envelopes (2–50 μm). The water droplets of the size typically found in freezing drizzle are classified as supercooled large droplets (SLDs). Dow provided an excellent overview of the accident and its causes in his 1995 article.[1]

Ice accretions that are due to large-droplet icing can occur on the upper surface behind the active portion of the deicing system boot and can lead to a spanwise-step type of ice accretion protuberance.[2] If the accretion occurs on the spanwise section of the wing where the aileron is located, it can alter the flow over the aileron and lead to changes in the lateral control and the associated hinge moment. It is this degradation in aileron control that is thought to have led to the Roselawn accident. Although the accident is thought to have occurred because of the presence of SLDs and subsequent loss of aileron control, the problem is more general. This type of ice accretion can also occur in supercooled droplet clouds of Appendix C size droplets when the air temperature is near freezing. In this case, the accretion occurs behind the boot because of surface water runback, and not because of impingement in this region. Also, spanwise-step-ice accretion is not limited to the wing and aileron, but could also occur on the horizontal and the vertical tails and affect the elevator and the rudder, respectively.

The influence of ice accretion behind deicing boots on aircraft performance has long been recognized. Wind-tunnel measurements by Johnson[3] in 1940 showed a 36% reduction in maximum roll control power that was due to ice accretion with full aileron deflection. As a response to a Viking aircraft incident, Morris,[4] in 1947, reported wind-tunnel results of the effect of simulated ice shapes on the leading edge of the aircraft horizontal tail. The objective was to propose a fix for the elevator control. One of the simulated ice shapes resembled a SLD accretion and was intended to represent ice formed downstream of a deicing system. Hinge-moment results were summarized, and design guidelines were presented. In 1948, Thoren[5] documented a 2-h test flight in freezing rain with a Lockheed P2V aircraft. During this encounter, runback and freezing were observed behind the boots. A considerable increase in section drag and a reduction in lift were noted, but no serious degradation in lateral control was experienced. Thus by 1950 it seems clear that there existed a basic understanding that ice accretion aft of the boots could affect aircraft control.

Research at the University of Wyoming has considered the aerodynamic effects of various types of ice accretion. During flight tests of a King Air aircraft, Cooper et al.[6] experienced two icing encounters with droplet sizes from 30 to 300 μm. Aircraft performance losses for these cases were "anomalously large although the liquid water content (LWC) and median volume diameter (MVD) did not indicate that these cases should have been potentially hazardous." Recently Ashenden and Marwitz[7] analyzed several Wyoming King Air flights in icing to determine the effect of various icing encounters on aircraft performance. They reported that freezing-drizzle exposure resulted in the maximum rate of performance degradation of all icing cases studied. Ashenden et al.[8] found a similar result in low-Reynolds-number two-dimensional wind-tunnel tests with simulated ice accretions. The results showed more severe aerodynamic penalties that were due to the freezing-drizzle case when operation of the deicing boot was simulated.

Initial insight into the effect of SLD ice accretion on aircraft control can be found in the excellent report on horizontal tail stall by Trunov and Ingelman-Sundberg.[9] The combination of increased downwash that was due to main wing flap deflection and decreased maximum lift and stall angle that were due to ice on the horizontal tail can lead to horizontal tail stall. They reported hinge-moment data on airfoils and tail sections with simulated Appendix C ice accretions and argued that the change in airfoil pressure distribution

Received 26 October 1998; revision received 27 March 1999; accepted for publication 3 April 1999.

*Graduate Research Assistant, Department of Aeronautical and Astronautical Engineering. Member AIAA.
†Professor, Department of Aeronautical and Astronautical Engineering. Associate Fellow AIAA.

over the elevator that was due to the ice-induced separation led to altered hinge moments and pilot control forces.

In 1996, Bragg[10,11] reviewed the aerodynamic effects of large-droplet ice accretion on aircraft aerodynamics and lateral control based in part on horizontal tail stall data.[9,12] The spanwise-step-ice accretion, thought to be typical of SLD ice, was shown not only to degrade lift and drag, but also to affect adversely the aileron hinge moment. This hinge-moment effect was traced to the change in the airfoil pressure distribution caused by the separation induced by the ice accretion. The authors were unaware of detailed aerodynamic data for spanwise-step-ice accretions (as is considered herein).

In view of the absence of such detailed data, some previous data with two-dimensional protuberances on an airfoil are relevant. Jacobs[13] in 1932 tested protuberances at different chordwise locations and varying heights on a NACA 0012 airfoil. The test revealed that the 5 and the 15% chord locations on the airfoil upper surface were the most sensitive in terms of lift and drag penalties for the large protuberance ($k/c = 0.0125$). In particular, this protuberance resulted in reductions in lift, as much as 68%, and a large change in pitching moment. However, no locations between 5 and 15% were tested, and the airfoil was not flapped. For smaller protuberances ($k/c < 0.005$), the effects were much less severe, and the most critical location was the leading edge. In 1956, Bowden[14] tested a small spanwise spoiler-type step protuberance of $k/c = 0.00286$ on a NACA 0011 airfoil at $x/c = 0.01$, 0.025, and 0.05. The test showed that the effects of the protuberance on lift and pitching moment became more severe as it was moved closer to the leading edge. The reduction in lift was as high as 20%. At angles of attack greater than 4 deg, the maximum increase in the drag was observed to occur when the protuberance was placed near the location of maximum local velocity. Recently, Calay et al.[15] tested three different small ($k/c = 0.0035$) simulated runback ice shapes at 5, 15, and 25% chords on a low-aspect-ratio NACA 0012 airfoil. The shapes at 5% had the largest effect on lift and drag, and the penalties were similar to those seen by Bowden.[14] The reports described do not provide the reasons why one protuberance size, shape, and location produced a more severe degradation in aerodynamic performance and control than another. This may have been due to the limited scope of the work that did not provide the authors enough information from which to draw any definitive conclusion.

As such, knowledge of spanwise-step-ice accretions and their effect on airfoil and aircraft performance and control is still limited. This paper presents the initial findings of a comprehensive experimental study of the aerodynamic effects of this type of simulated ice for k/c values of 0.0083 and 0.0139. The simple quarter-round ice simulations used were intended to produce the important two-dimensional aerodynamic effects of ice accretions but do not necessarily simulate the quantitative performance changes that would occur on a real three-dimensional ice accretion. The study examined the sensitivity of airfoil lift, drag, pitching moment, and flap-hinge moment to different chordwise locations and size of the ice simulations. The purpose was not only to identify the critical conditions under which the iced airfoil aerodynamics and flap-hinge moment rapidly diverge from the noniced case, but also to understand the aerodynamics that determine these conditions.

Experimental Method

The tests were performed in the University of Illinois $3' \times 4'$ Subsonic Wind Tunnel. An 18-in. chord modified NACA 23012 model (described in more detail in Ref. 16) with a 25% chord simple flap was used. The NACA 23012 airfoil was chosen because it has aerodynamic characteristics that are typical of the current commuter aircraft fleet.

Figure 1 shows the schematic of the experimental setup. The leading edge of the flap was located at $x/c = 0.75$. The flap-hinge axis was located at $x/c = 0.779$ and $y/c = 0.0049$. The model was attached to a three-component balance, which was also used to set the angle of attack. The flap was actuated by a two-arm linkage system, which was driven by a linear traverse. The traverse was mounted on the metric force plate of the balance. A load cell was attached in one of the arms and measured the flap-hinge moment. The model had 50

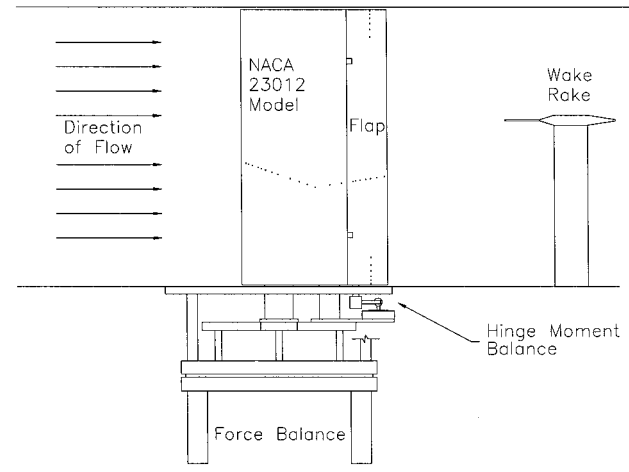

Fig. 1 Schematic of the experimental setup.

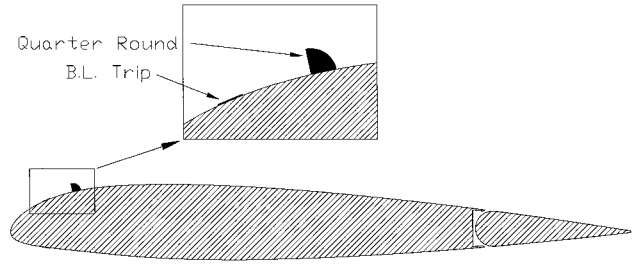

Fig. 2 NACA 23012 model with quarter-round ice simulation (0.25-in. quarter round at x/c = 0.10 shown). B.L., boundary layer.

surface-pressure taps on the main element and 30 surface-pressure taps on the flap (including 12 spanwise taps). A traversable wake rake with 59 total-pressure probes was used to measure the wake rake pressures from which the drag was determined. The pressures were measured with an electronically scanned pressure (ESP) system.

The lift coefficient C_l and pitching-moment coefficient C_m measurements about the quarter chord were derived from both the force balance and the surface-pressure measurements. In this paper only the values from the pressure measurements are shown for simplicity. The drag coefficient C_d measurements were taken with the wake rake by use of a momentum-deficit method. The flap-hinge-moment coefficients C_h were measured with the flap-hinge load cell and confirmed with the surface-pressure measurements. Fluorescent surface oil flow visualization was used to determine the boundary-layer state of the airfoil (such as boundary-layer transition and flow separation). The C_l, C_m, and C_d measurements were calculated by standard methods with conventional definitions. C_h was obtained by determination of the trailing-edge-down moment about the flap-hinge line and nondimensionalizing by the flap surface area and the flap chord length. All of the aerodynamic coefficients were corrected for wall effects by use of the method described by Rae and Pope.[17]

The spanwise-step-ice accretions were simulated with wooden quarter-round shapes. This is shown in Fig. 2. For selected cases, the boundary layer was tripped at $x/c = 0.05$ on both the upper and the lower surfaces with 0.012-in.-diam microbeads that were applied onto a 0.003-in.-thick and 0.25-in.-wide double-sided tape. The minimum flap gap was 0.06 in. on the upper surface and 0.08 in. on the lower surface. The tests were conducted with the flap gap unsealed.

All of the measurements (both the balance and the pressure) were taken at 50 Hz for 2 s and then time averaged. The force balance data were low-pass filtered at 1 Hz. None of the other measurements were filtered. A typical run consisted of sweeping the angle of attack from negative stall to a few degrees past positive stall in 1-deg increments.

Shown in Table 1 are the uncertainty estimates of the aerodynamic coefficients for a typical data point. The case shown is that of the clean model at $\alpha = 5$ deg with zero flap deflection and $Re = 1.8 \times 10^6$. The relative uncertainties for C_m and C_h appear to be rather large, but this was due to relatively small reference values

Table 1 Experimental uncertainties for the clean model at $\alpha = 5$ deg, $Re = 1.8 \times 10^6$

Aerodynamic coefficient	Reference value	Absolute uncertainty	Relative uncertainty, %
C_l pressure	0.633	2.11×10^{-03}	0.33
C_d wake	0.01022	1.43×10^{-04}	1.40
C_m pressure	−0.00894	3.49×10^{-04}	3.90
C_h balance	−0.0157	3.55×10^{-03}	9.70

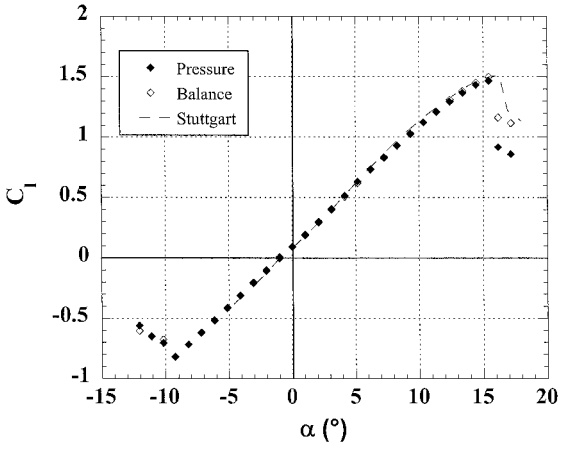

Fig. 3 Comparisons of clean NACA 23012 lift measurements between present University of Illinois at Urbana–Champaign (UIUC) data (balance and pressure) and those of Stuttgart[18] (UIUC $Re = 1.8 \times 10^6$; Stuttgart $Re = 2.0 \times 10^6$).

at this point. The clean-model baseline measurements were taken and compared with the published experimental measurements of Althaus and Wortmann[18] at the University of Stuttgart. The measurements compared favorably and validated the experimental apparatus and data reduction methods of this study. The lift comparison is shown in Fig. 3.

Results

In this section, the C_l and C_m data were taken from the integrated surface pressures and the C_d measurements were taken from the wake-pressure data. The flap-hinge-moment balance measurements were used to generate the C_h data. The integrated aerodynamic coefficient values are presented first. Then, by use of surface flow visualization and pressure data, the flowfield is analyzed to provide a better understanding of the effect of the simulated ice.

Effect of Simulated Ice Shape Location

Figure 4 shows the effect of the 0.25-in. ($k/c = 0.0139$) simulated ice shape at three different x/c locations on the aerodynamic coefficients. The boundary layer was tripped at 5% chord (upper and lower surface) for the cases with the simulated ice shapes at $x/c = 0.10$ and 0.20. All of the simulated ice cases showed reduced lift curve slopes in the linear regions ($-5 < \alpha < 1$) when compared with the clean case (Fig. 4a). The simulated-ice cases also exhibited gradual stall characteristics typical of a thin-airfoil-type stall. The simulated ice shapes dramatically reduced the $C_{l,\max}$, with the worst case (of the three cases shown) being a $C_{l,\max}$ of 0.32 when the simulated ice was at $x/c = 0.10$. The $C_{l,\max}$ increased to 0.56 when the simulated ice shape was moved upstream to $x/c = 0.02$ and to 0.42 when it was moved downstream to $x/c = 0.20$. The $x/c = 0.10$ case had $\alpha_{\text{stall}} = 6$ deg, which was the lowest of the three simulated ice shape cases shown. It is shown below that the worst ice shape location for $C_{l,\max}$ degradation was at $x/c = 0.12$.

Figure 4b shows the drag polars with the 0.25-in. simulated-ice shape at the three different x/c locations. Results are not shown for angles near $C_{l,\max}$ and beyond, where large regions of flow separation on the airfoil bring the wake survey method into question. Figure 4b shows significant increases in drag when the simulated ice shape was present. The largest increase in drag for $C_l > 0$ occurred when the simulated ice shape was at $x/c = 0.10$, which also corresponds to the case with the lowest $C_{l,\max}$. However, at $C_l < 0$, the largest increase in drag occurred when the simulated ice shape was located at $x/c = 0.20$.

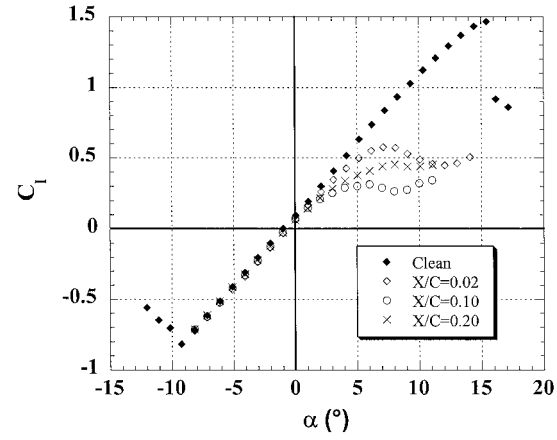

Fig. 4a Effects of 0.25-in. simulated ice shape on lift. Boundary layer tripped at 5% chord for $x/c = 0.10$ and 0.20 cases, $Re = 1.8 \times 10^6$.

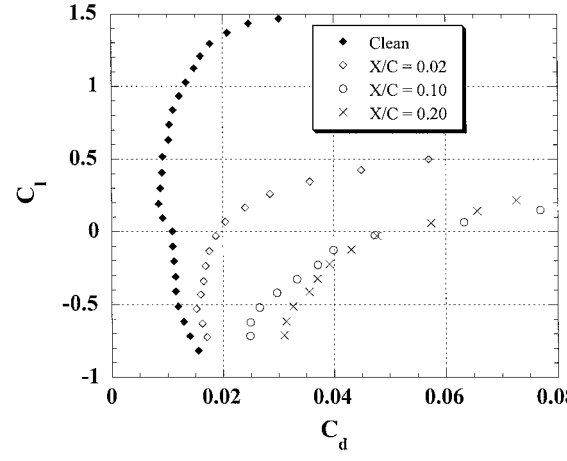

Fig. 4b Effects of 0.25-in. simulated ice shape on drag. Boundary layer tripped at 5% chord for $x/c = 0.10$ and 0.20 cases, $Re = 1.8 \times 10^6$.

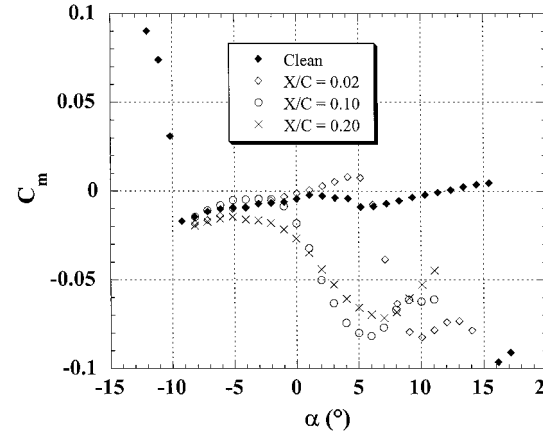

Fig. 4c Effects of 0.25-in. simulated ice shape on pitching moment. Boundary layer tripped at 5% chord for $x/c = 0.10$ and 0.20 cases, $Re = 1.8 \times 10^6$.

The pitching moments with the three simulated ice shape locations are shown in Fig. 4c. When the simulated ice shape was at $x/c = 0.10$ and 0.20, the pitching moment exhibited a large break in the slope at $\alpha = -1$ deg, becoming more negative, indicating that the airfoil was more aft loaded. When the simulated ice shape was located at $x/c = 0.02$, the pitching moment diverged at $\alpha = 5$ deg.

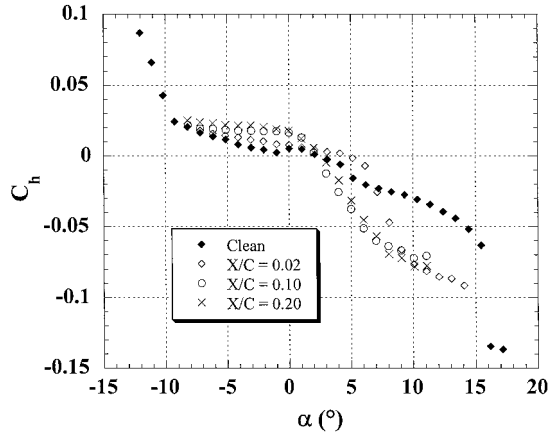

Fig. 4d Effects of 0.25-in. simulated ice shape on flap-hinge moment. Boundary layer tripped at 5% chord for $x/c = 0.10$ and 0.20 cases, $Re = 1.8 \times 10^6$.

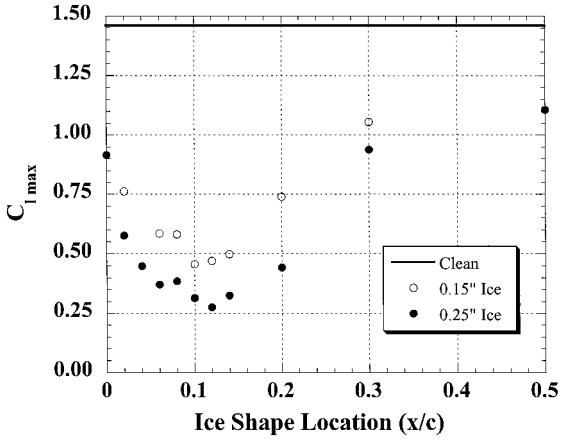

Fig. 5 Summary of $C_{l,\max}$ with simulated ice shape at various x/c locations. Boundary layer tripped at 5% chord for $x/c \geq 0.08$, $Re = 1.8 \times 10^6$.

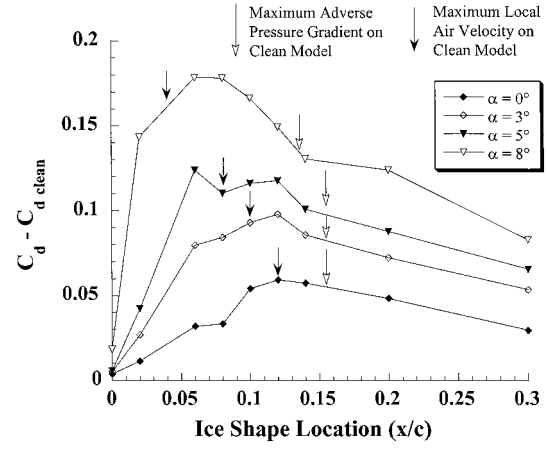

Fig. 6 Drag increase due to 0.25-in. simulated ice shape. Boundary layer tripped at 5% chord for $x/c \geq 0.08$, $Re = 1.8 \times 10^6$.

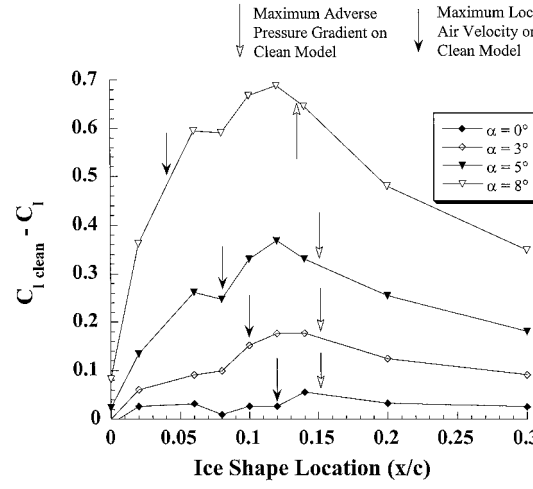

Fig. 7 Lift loss due to 0.25-in. simulated ice shape. Boundary layer tripped at 5% chord for $x/c \geq 0.08$, $Re = 1.8 \times 10^6$.

However, between $\alpha = 0$ and 5 deg, the pitching moment was more positive than the clean case. Figure 4d shows the flap-hinge moments with the simulated ice shape at the three different x/c locations. Between $\alpha = -9$ and 1 deg, the hinge moments with the simulated ice shape present were higher than that of the noniced case, indicating a larger trailing-edge-down moment about the flap hinge. The cases with the simulated ice shape at $x/c = 0.10$ and 0.20 exhibited a large break in the slope at $\alpha = 0$ deg. The case with the simulated ice shape at $x/c = 0.02$ exhibited a large break in the slope $\alpha = 6$ deg. Figures 4c and 4d show that the sudden divergence in the flap-hinge moment occurred at an angle of attack that was a few degrees higher than that of the pitching moment.

Figure 5 shows the summary of $C_{l,\max}$ versus x/c location for the two simulated ice shapes tested as well as the clean airfoil $C_{l,\max}$ with natural transition. All of the cases with the simulated ice shapes at or downstream of 8% chord had the boundary layer tripped at 5% chord (upper and lower surface). The cases with the simulated ice shapes upstream of 8% chord were not tripped. This caused the slight discontinuity in the curves at $x/c = 0.08$. The lowest $C_{l,\max}$ for the 0.25-in. shape ($k/c = 0.0139$) was 0.27 and occurred at $x/c = 0.12$. The lowest $C_{l,\max}$ for the 0.15-in. shape ($k/c = 0.0083$) was 0.45 and occurred at $x/c = 0.10$. The maximum lift increased rapidly as the simulated ice was moved forward of this location, reaching 0.92 at the leading edge for the 0.25-in. case. The $C_{l,\max}$ for the 0.15-in. cases were higher than that for the 0.25-in. case at all x/c locations. Thus it is clear from Fig. 5 that in terms of maximum lift loss, the most critical location for the simulated ice shapes tested was near $x/c = 0.12$.

As stated in the Introduction, studies[13–15] have shown that the effects of spanwise surface protuberance (of $k/c < 0.005$) on lift, drag, and pitching moment became more severe as it was moved closer to the leading edge. Gregory and O'Reilly[19] showed that the $k/c = 0.0004$ surface roughness resulted in the most severe loss in $C_{l,\max}$ (on a NACA 0012 airfoil) when it was placed at the leading edge. Bowden[14] observed that the maximum increases in the drag occurred when the protuberance was located near the location of maximum local surface velocity (or minimum C_p). A possible explanation for this is that the protuberance would extract the greatest amount of boundary-layer momentum when placed at that location, which would thicken the boundary layer and increase drag. Figure 6 shows the drag increase (compared with the clean airfoil) that is due to the 0.25-in. ice shape simulation. Each curve represents a fixed angle of attack, and the simulated ice shape location is depicted on the x axis. Also indicated in the figure by the solid arrows are the locations of maximum local air velocity (of the clean airfoil) for each angle of attack and by the open arrows are the location of the maximum adverse pressure gradient (also of the clean airfoil). The figure shows that as the angle of attack was increased, the chordwise location with the greatest increase in drag moved upstream and was approximately at the location of the maximum local air velocity. This is similar to what Bowden[14] found on a NACA 0011 airfoil.

However, as shown in Fig. 7, the loss in lift that was due to the 0.25-in. ice shape simulation did not follow this behavior. The figure shows that there were maxima in the lift loss as well. However, unlike the drag increase, the simulated ice shape location for maximum lift loss was well downstream of the maximum local air velocity and slightly upstream of the maximum adverse pressure gradient. Also, the maxima remained fixed near $x/c = 0.12$ and did not move upstream with increasing angles of attack. This was the same x/c location that produced the lowest $C_{l,\max}$ as shown in Fig. 5. A detailed analysis of the data of Jacobs[13] by the authors also showed that for the large ($k/c = 0.0125$) protuberance, the largest lift loss

also occurred when it was located well downstream of the maximum local air velocity in the adverse pressure region. Thus it is apparent that for the large protuberances tested here, the chordwise location with the most severe reduction in lift did not coincide with either the location of the maximum adverse pressure gradient or the local maximum air velocity (although it was bounded by them). However, for this airfoil, the location of the maximum adverse pressure gradient seemed to be a better indicator.

Flowfield Analysis

The flowfield is discussed in this subsection to provide a better understanding of the integrated results of the preceding subsection. Figure 8 summarizes the boundary-layer state observed on the model by use of fluorescent oil flow visualization and shows the progression of the separation bubbles upstream and downstream of the ice shape simulation as the angle of attack was increased. Here, the 0.25-in. quarter-round ice simulation was located at $x/c = 0.10$. The primary separation bubble upstream of the simulated ice shape formed at $x/c = 0.07$ at $\alpha = 0$ deg. The separation point moved gradually upstream to $x/c = 0.05$ at $\alpha = 3$ deg and remained at this location to $\alpha = 5$ deg. Evidence of a secondary separation bubble upstream of the simulated ice shape was observed but was not shown because it could not be accurately measured. The primary downstream bubble reattachment region was located between $x/c = 0.40$ and 0.44 at $\alpha = 0$ deg. It was not clearly defined because the reattachment of the ice-induced bubble was seen in the oil flow as a band of relatively stagnant oil on the surface. The stagnant oil band was probably an indication of an unsteady reattachment process. The region moved downstream as α was increased and at $\alpha = 3.25$ deg was located between $x/c = 0.75$ and the trailing edge. Thus, for the 0.25-in. quarter round at $x/c = 0.10$, the stall was initiated by a rapidly growing separation bubble that eventually reached the trailing edge, which is characteristic of a thin-airfoil stall. There was no evidence from flow visualization of a trailing-edge separation.

The large change in the flowfield around the airfoil can be seen in the pressure distribution plots of Figs. 9 and 10. Figure 9 shows the surface-pressure distribution with the 0.25-in. ice shape simulation placed at various chordwise locations at $\alpha = 0$ deg and compared with the clean case. The clean case shows the stagnation point at the leading edge with a suction peak at $x/c = 0.12$ on the upper surface and at $x/c = 0.02$ on the lower surface. There is a discontinuity in the C_p at $x/c = 0.78$ that is due to the flap gap. On a clean NACA 23012 airfoil, over 50% of the lift is generated in the first 25% of the chord.

The pressure distributions with the simulated ice shape downstream of $x/c = 0$ show a severely altered flowfield, even at this angle of attack. It is first important to note that the surface pressure was not measured over the simulated ice shape. Thus the C_p from the last pressure tap upstream of the simulated ice shape is connected to the first pressure tap downstream of the simulated ice shape by a straight line. When the simulated ice shape location was at the leading edge of the model, the pressure distribution was nearly identical to that of the clean model. The flowfield started to become significantly altered when the simulated ice shape was at $x/c = 0.02$. There was a large suction peak ($C_p = -1.20$) immediately downstream of the simulated ice shape as the flow accelerated

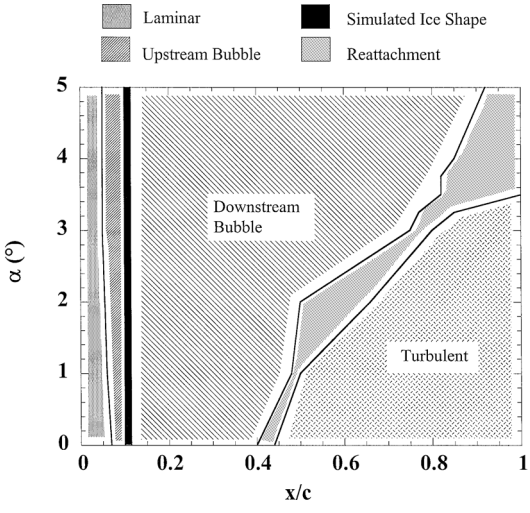

Fig. 8 Summary of boundary-layer state with 0.25-in. simulated ice shape at $x/c = 0.10$ obtained from flow visualization. Natural transition. $Re = 1.8 \times 10^6$.

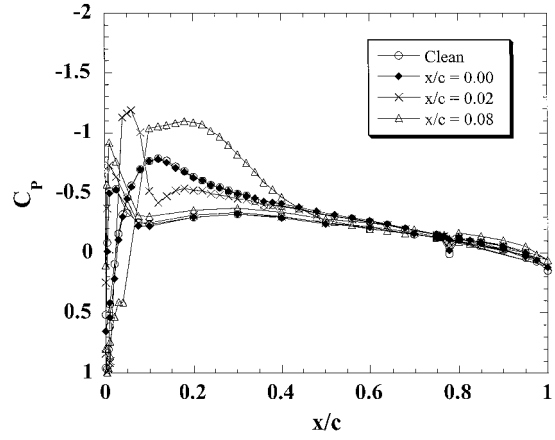

Fig. 9a Effect of 0.25-in. simulated ice shape at various locations on pressure distribution. Boundary layer tripped at 5% chord for $x/c \geq 0.08$, $\alpha = 0$ deg, $Re = 1.8 \times 10^6$.

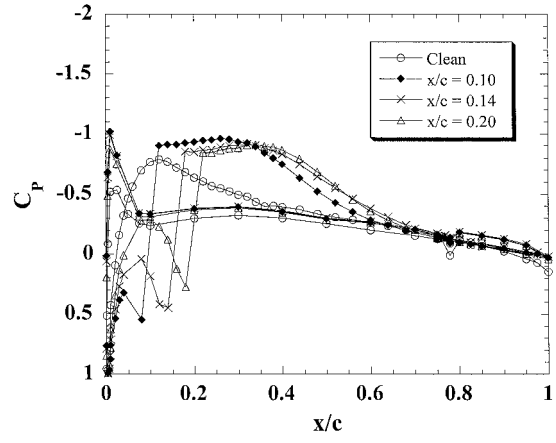

Fig. 9b Effect of 0.25-in. simulated ice shape at various locations on pressure distribution. Boundary layer tripped at 5% chord for $x/c \geq 0.08$, $\alpha = 0$ deg, $Re = 1.8 \times 10^6$.

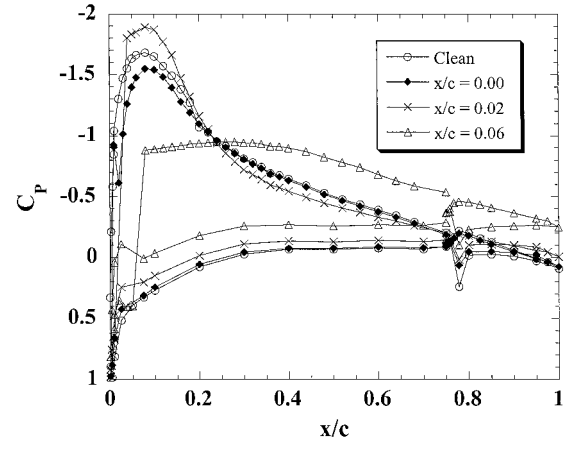

Fig. 10a Effect of 0.25-in. simulated ice shape at various locations on pressure distribution. Boundary layer tripped at 5% chord for $x/c \geq 0.08$, $\alpha = 5$ deg, $Re = 1.8 \times 10^6$.

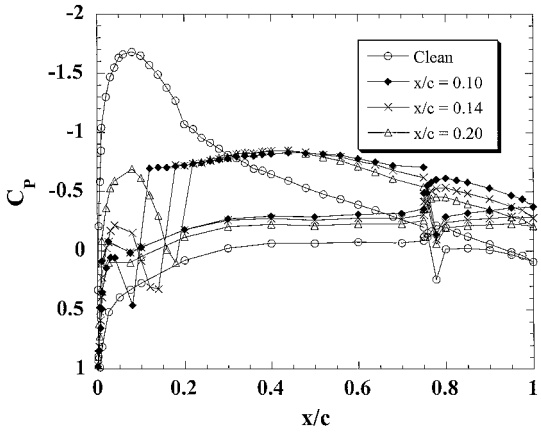

Fig. 10b Effect of 0.25-in. simulated ice shape at various locations on pressure distribution. Boundary layer tripped at 5% chord for $x/c \geq 0.08$, $\alpha = 5$ deg, $Re = 1.8 \times 10^6$.

over it and separated. However, the simulated ice shape was located in a very favorable pressure gradient and the bubble was able to reattach quickly at $x/c = 0.10$. This allowed another suction peak (primarily because of the airfoil geometry and not the simulated ice shape) to form at $x/c = 0.18$ with a C_p value of -0.51.

When the simulated ice shape was located at $x/c = 0.06$, the flow on the upper surface initially accelerated from the leading-edge stagnation point. However, the flow started to decelerate as it approached the simulated ice shape and experienced an adverse pressure gradient and flow separation. This resulted in a local $C_{p,\min}$ of 0.52 located ahead of the simulated ice shape at $x/c = 0.03$, followed by a $C_{p,\max}$ of 0.58 at $x/c = 0.04$. Immediately downstream of the simulated ice shape, a longer separation bubble was formed and the C_p was nearly constant at -1.15 until $x/c = 0.15$, where it started to increase as the reattachment process began. Near $x/c = 0.32$, the C_p approached the clean-model value and indicated that the flow had reattached. Although the simulated ice shape was located in a favorable pressure gradient, it was so close to the location of the onset of adverse pressure gradient that the separation bubble was forced to reattach in an adverse pressure gradient. Thus the separation bubble for this simulated ice shape location was much larger than when the simulated ice shape was located at $x/c = 0.02$.

With the simulated ice shape located at $x/c = 0.10$, the local $C_{p,\min}$ and $C_{p,\max}$ upstream of the simulated ice shape became more clearly defined as there was a greater surface length along the model for the flow first to accelerate and then decelerate upstream of the simulated ice shape. In this case, the simulated ice shape was located near the clean-airfoil suction peak and all of the separation bubble was located in the clean-airfoil adverse pressure gradient region. This resulted in a very large separation bubble that did not reattach until near $x/c = 0.65$. (This is quite different from what was shown in Fig. 8 because there was a significant difference in the bubble length between the tripped and the untripped cases. The tripped cases generally had a ~20% longer separation bubble length, and subsequently the effects of the ice shape were more severe. In the fluorescent oil flow visualization, the boundary layer was not tripped. However, in the pressure distribution plot of Fig. 9, as well as in all of the other figures, the boundary layer was tripped.) When the simulated ice shape was moved downstream to $x/c = 0.14$ and 0.20, both the simulated ice shape and the separation bubble were located in a region of adverse pressure gradient. It is interesting to note that the pressure distribution in the separated regions of these two cases appear almost identical. In both of the cases, the C_p value at the constant-pressure region downstream of the simulated ice shape was approximately -0.80 and the reattachment process occurred near $x/c = 0.75$. Thus the separation bubble length actually decreased when the simulated ice shape was moved from $x/c = 0.14$ to 0.20. Note also that the trailing-edge pressure was the lowest when the simulated ice shape was located at $x/c = 0.14$, indicating the least upper-surface-pressure recovery.

The separation bubbles described above (especially when the simulated ice shape was located downstream of $x/c = 0.02$) were very similar to the long laminar separation bubble described by Tani.[20] The overall shapes of the pressure distributions were very similar to those observed by Mullins et al.[12] and Calay et al.[15] However, the length of the separation bubble for this investigation was much longer because the simulated ice used in this test was much larger. The shape of the pressure distribution when the simulated ice shape was located at $x/c = 0.02$ compared very favorably with that observed by Bragg et al.,[21] who performed extensive measurements on a NACA 0012 airfoil with a large leading-edge ice shape.

As Fig. 10 shows, similar trends in the pressure distributions were observed for $\alpha = 5$ deg. This was approximately the angle of attack at which $C_{l,\max}$ occurred for many of the cases with a simulated ice shape. The pressure distribution for the clean case shows a suction peak ($C_p = -1.7$) at $x/c = 0.08$. Well over half of the lift occurred in the first 25% chord because of the large leading-edge suction. When the simulated ice shape was placed at the leading edge, a very small separation bubble formed that reattached by $x/c = 0.02$. The extremely small separation bubble was due to the very favorable pressure gradient in which the simulated ice shape was located. Downstream of the reattachment location, the pressure distribution was similar to the clean case. However, the suction peak (beacuse of the airfoil geometry) was not as large. When the simulated ice shape was at $x/c = 0.02$, the C_p in the separation bubble downstream of the simulated ice shape was even more negative than that of the clean-model suction peak. The simulated ice shape was still located in a favorable pressure gradient and, although the resulting separation bubble was longer than that of the case with the simulated ice shape located at the leading edge, it was still relatively short.

When the simulated ice shape was located at $x/c = 0.06$, a very long separation bubble formed downstream of the simulated ice shape. In fact, the large suction peak that normally forms near $x/c = 0.08$ was completely replaced with this separation bubble. This was the case in which the simulated ice shape was located near the suction peak of the clean model and almost all of the resulting separation bubble was located in the adverse pressure region. It was difficult to determine from the surface-pressure values whether or not the separation bubble reattached. However, it was likely that the bubble was unsteady and was intermittently attached at the trailing edge. When the simulated ice shape was located at and downstream of $x/c = 0.06$, the resulting separation bubbles were very similar, with nearly identical C_p values. In these cases all or the majority of the separation bubble was located in the adverse pressure gradient of the clean model. This was also observed at $\alpha = 0$ deg, as Fig. 9 shows. As the simulated ice shape was moved downstream from the leading edge to $x/c = 0.20$, the local suction peak upstream of the simulated ice shape grew. Again the $x/c = 0.10$ case shows the least upper-surface-pressure recovery as shown by the trailing-edge pressures.

Airfoil Performance Analysis

It is apparent from the flow visualization and pressure distribution plots that the large loss in lift observed in Fig. 7 was due to the long separation bubble that formed downstream of the simulated ice shape. Figure 9 shows that the long separation bubbles formed when the simulated ice shape was located in the vicinity of and downstream of the suction peak (of the clean airfoil) in the pressure recovery region. This was because the separation bubble was unable to reattach quickly in the adverse pressure gradient. When this occurred, the large suction peak observed on the clean airfoil (where the bulk of the lift was generated) was eliminated. However, when the simulated ice shape was located far enough downstream, a smaller local suction region was able to form upstream of the simulated ice shape, recovering some of the lift.

When the pressure distribution is examined, the trends seen in the integrated pitching and flap-hinge moments of Fig. 4 can be better understood. NACA 23012 is a forward-loaded airfoil in which most of the lift is generated in the vicinity of the large suction peak that forms near the leading edge of the airfoil. At $\alpha = 0$ deg, when the simulated ice shape was located at $x/c = 0.10$ and 0.20, most of the lift was generated in the region of the long separation bubble that formed downstream of the simulated ice shape. In fact, negative lift was generated upstream of the simulated ice shape. Thus it became

more aft loaded than the clean airfoil. When the simulated ice shape was located at $x/c = 0.02$, most of the lift was also generated by the separation bubble. However, the separation bubble was very short and it was located upstream of the quarter-chord location, resulting in a more front-loaded lift distribution than that of the clean airfoil. This can be seen in Fig. 4c, which shows that at $\alpha = 0$ deg, when the simulated ice shape was located at $x/c = 0.02$, C_m was more positive (or nose up) than that of the clean case. However, when the simulated ice shape was located at $x/c = 0.10$ and 0.20, the pitching moments were more negative than the clean case at this angle of attack.

Similar trends were observed at $\alpha = 5$ deg. Figure 10 shows that when the simulated ice shape was located at $x/c = 0.10$ and 0.20, the large suction peak near the leading edge of the airfoil was essentially eliminated and a long separation bubble formed downstream of the simulated ice shape. Thus the airfoil became much more aft loaded. When the simulated ice shape was located at $x/c = 0.02$, the suction peak that formed near the leading edge of the model was even larger than that of the clean case. Thus the airfoil became more front loaded than the clean case. Again, the result of the large changes in the pressure distribution that were due to the simulated ice can be observed in the measured pitching moments of Fig. 4c.

Figure 9 shows that at $\alpha = 0$ deg, the presence of the simulated ice shapes did not significantly alter the pressure distribution over the flap. However, as shown in Fig. 4d, when the simulated ice shape was located at $x/c = 0.10$ and 0.20, the effect of the simulated ice shape was large when based on the clean value, even though the changes are small in an absolute sense. At this angle of attack ($\alpha = 0$ deg), the simulated ice shape unloaded the flap (i.e., made C_h more positive). The relatively small absolute changes in C_h at this angle of attack may have been due to all of the separation bubbles' reattaching upstream of the flap. However, at $\alpha = 5$ deg, the separation bubble did reach the flap when the simulated ice shape was located at and downstream of $x/c = 0.06$. This resulted in a much larger pressure difference between the upper and the lower surfaces of the flap (Fig. 10), when compared with that the clean case. Figure 4d shows that at $\alpha = 5$ deg, the C_h for $x/c = 0.10$ and 0.20 cases were more than twice as negative as that of the clean case. (An interesting result is that when the simulated ice shape was located at $x/c = 0.02$, C_h was nearly zero.) Thus from the analysis of the pressure distribution, it is apparent that the sudden break in the C_h curves observed in Fig. 4d was due to the separation bubble's reaching the flap.

Conclusions

An experimental investigation was conducted to study the aerodynamic effect of simulated spanwise ice shapes with height-to-chord ratios of 0.0083 and 0.0139 on a modified NACA 23012 airfoil. The following conclusions can be drawn:

1) Simulated spanwise ice accretion severely reduced $C_{l,\max}$. The most critical simulated ice shape location (in terms of reduction in $C_{l,\max}$) was 12% chord for a forward-facing quarter round with height-to-chord ratio of 0.0139. It resulted in a $C_{l,\max}$ of 0.27 compared with an uniced airfoil $C_{l,\max}$ of 1.46.

2) The simulated ice shape produced a large separation bubble, drastically changed the airfoil pressure distributions, and changed the airfoil stall type from leading-edge to thin-airfoil stall.

3) The simulated ice shape severely altered pitching and flap-hinge moments. A large break in $C_{h,\alpha}$ was observed a few degrees angle of attack after a break in $C_{m,\alpha}$. This resulted in a large nose down, the trailing edge up, pitching, and flap-hinge moments that were generated well before and continued through stall.

4) The most critical location of the simulated ice shape (in terms of loss in lift for a given α) was near (but upstream of) the location of largest adverse pressure gradient of the clean airfoil and downstream of the location of the minimum surface pressure.

5) The severe loss in lift at a positive angle of attack was due to the simulated ice shape's preventing the suction peak from forming near the leading edge. Most of the lift on a clean NACA 23012 is generated in this suction peak. When the simulated ice shape was at critical chordwise locations, this suction peak was eliminated by a long separation bubble, which formed downstream of the simulated ice shape.

6) The separation bubble failed to reattach at angles of attack as low as 5 deg, which led to the very low $C_{l,\max}$ values observed.

Acknowledgments

This work was supported by the Federal Aviation Administration (FAA) under grant DTFA MB 96-6-023 with James Riley as technical monitor. The authors also thank Gene Hill from the FAA and Tom Bond and Mark Potapczuk from NASA. Eric Loth and Tim Dunn from the University of Illinois at Urbana–Champaign (UIUC) made significant contributions to our understanding of this flow through their computational fluid dynamics (CFD) calculations, and Holly Gurbacki of UIUC contributed to both the CFD and the experimental study.

References

[1]Dow, J. P., Sr., "Roll Upset in Severe Icing," Federal Aviation Administration, Aircraft Certification Service, Washington, DC, Sept. 1995.

[2]National Transportation Safety Board, "Icing Tanker Test Factual Report," Docket SA-512, Exhibit 13B, DCA95MA001, Washington, DC, Feb. 1995.

[3]Johnson, C. L., "Wing Loading, Icing and Associated Aspects of Modern Transport Design," *Journal of the Aeronautical Sciences*, Vol. 8, No. 2, 1940, pp. 43–54.

[4]Morris, D. E., "Design to Avoid Dangerous Behavior of an Aircraft Due to the Effects on Control Hinge Moments of Ice on the Leading Edge of the Fixed Surface," Aeronautical Research Council, TN Aero. 1878, CP 66, London, March 1947.

[5]Thoren, R. L., "Icing Flight Tests on the Lockheed P2V," ASME Paper 48-SA-41, American Society of Mechanical Engineers, New York, 1948.

[6]Cooper, W. A., Sand, W. R., Politovich. M. K., and Veal, D. L., "Effect of Icing on Performance of a Research Airplane," *Journal of Aircraft*, Vol. 21, No. 9, 1984, pp. 708–715.

[7]Ashenden, R., and Marwitz, J., "Turboprop Aircraft Performance Response to Various Environmental Conditions," *Journal of Aircraft*, Vol. 34, No. 3, 1997, pp. 278–287.

[8]Ashenden, R., Lindberg, W., and Marwitz, J., "Two-Dimensional NACA 23012 Airfoil Performance Degradation by Super Cooled Cloud, Drizzle, and Rain Drop Icing," AIAA Paper 96-0870, Jan. 1996.

[9]Trunov, O. K., and Ingelman-Sundberg, M., "On the Problem of Horizontal Tail Stall Due to Ice," Rept. JR-3, The Swedish Soviet Working Group on Scientific-Technical Cooperation in the Field of Flight Safety, Norrkoping, Sweden, 1985.

[10]Bragg, M. B., "Aircraft Aerodynamic Effects Due to Large Droplet Ice Accretions," AIAA Paper 96-0932, Jan. 1996.

[11]Bragg, M. B., "Aerodynamics of Supercooled-Large-Droplet Ice Accretion and the Effect on Aircraft Control," *Proceedings of the FAA International Conference on Aircraft Inflight Icing*, Vol. 2, DOT/FAA/AR-96/81, II, Federal Aviation Administration, Washington, DC, 1996, pp. 387–399.

[12]Mullins, B. R., Smith, D. E., and Korkan, K. D., "Effect of Icing on the Aerodynamic Performance of a Flapped Airfoil," AIAA Paper 95-0449, Jan. 1995.

[13]Jacobs, E. N., "Airfoil Section Characteristics as Affected by Protuberances," NACA Rept. 446, 1932.

[14]Bowden, D. T., "Effect of Pneumatic De-Icers and Ice Formations on Aerodynamic Character of an Airfoil," NACA TN 3564, Feb. 1956.

[15]Calay, R. K., Holdù, A. E., and Mayman, P., "Experimental Simulation of Runback Ice," *Journal of Aircraft*, Vol. 34, No. 2, 1997, pp. 206–212.

[16]Lee, S., Dunn, T., Gurbacki, H. M., Bragg, M. B., and Loth, E., "An Experimental and Computational Investigation of Spanwise-Step-Ice Shapes on Airfoil Aerodynamics," AIAA Paper 98-0490, Jan. 1988.

[17]Rae, W. H., and Pope, A., *Low-Speed Wind Tunnel Testing*, Wiley, New York, 1984, pp. 349–362.

[18]Althaus, D., and Wortmann, F., "Experimental Results from the Laminar Wind Tunnel of the Institute for Aerodynamic and Gasdynamics—The University of Stuttgart," Dept. of Mechanical and Aerospace Engineering, Princeton Univ., Princeton, NJ, 1979, pp. 316, 317.

[19]Gregory, N., and O'Reilly, C. L., "Low-Speed Aerodynamic Characteristics of NACA 0012 Aerofoil Section, Including the Effects of Upper-Surface Roughness Simulating Hoar Frost," ARC R&M 3726, NASA Ames Research Center, Jan. 1970.

[20]Tani, I., "Low Speed Flows Involving Bubble Separations," *Progress in Aeronautical Sciences*, Pergamon, New York, 1964, pp. 70–103.

[21]Bragg, M. B., Khodadoust, A., and Spring, S. A., "Measurements in a Leading-Edge Separation Bubble Due to a Simulated Airfoil Ice Accretion," *AIAA Journal*, Vol. 30, No. 6, 1992, pp. 1462–1467.